Journal of Materials Chemistry A

Accepted Manuscript

ROYAL SOCIETY OF CHEMISTRY

www.rsc.org/materialsA

Graphic Abstract

A Novel In-situ Preparation Method of Nanostructured α-Fe_2O_3 Films from Electrodeposited Fe Films for Efficient Photoelectrocatalytic Water Splitting and Organic Pollutant Degradation

Qingyi Zeng, Jing Bai, Jinhua Li, LigangXia, Ke Huang, Xuejin Li and Baoxue Zhou*[a]

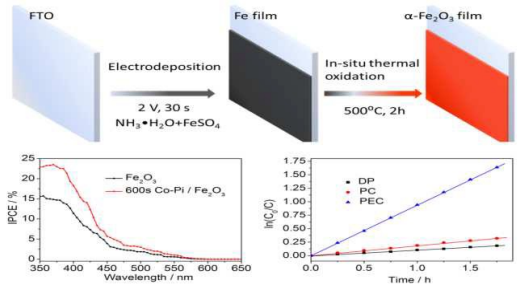

Highly photoactive α-Fe_2O_3 films prepared from novel electrodeposited Fe films were reported for PEC water splitting and organic pollutant degradation.

School of Environmental Science and Engineering, Shanghai Jiao Tong University, No. 800 Dongchuan Rd, Shanghai 200240 PR China.
E-mail: zhoubaoxue@sjtu.edu.cn; Fax: (+86)21-54747351

Journal of
Materials Chemistry A

RSCPublishing

PAPER

A Novel In-situ Preparation Method of Nanostructured α-Fe_2O_3 Films from Electrodeposited Fe Films for Efficient Photoelectrocatalytic Water Splitting and Organic Pollutant Degradation

Cite this:

Received ,
Accepted

DOI:

www.rsc.org/ees

Qingyi Zeng, Jing Bai, Jinhua Li, LigangXia, Ke Huang, Xuejin Li and Baoxue Zhou*

A novel preparation method was reported for preparing nanostructured hematite (α-Fe_2O_3) films used in efficient photoelectrocatalytic (PEC) water splitting and organic pollutant degradation. The method includes two processes, namely the electrodeposition of Fe films in alkalescent aqueous electrolyte with ferrisulfas and ammonia and the in-situ thermal oxidation of Fe films to obtain α-Fe_2O_3 films. The thickness and crystallinity of the α-Fe_2O_3 films can be precisely controlled by adjusting electrodeposition durations and annealing conditions, respectively, and the microstructured defects from traditional electrodeposition of FeOOH films and the undesired phases of FeO and/or Fe_3O_4 from thermal oxidation of Fe foils can be avoided, which facilitates the generation and transport/collection of photo-generated charges in the as-prepared α-Fe_2O_3 films. The optimized α-Fe_2O_3 film, which was obtained from a Fe film deposited for 30 s and then annealed at 500 ºC for 2 h, showed a stable PEC water oxidation current of ~1.35 mA cm^{-2} at 1.23 V (*vs.* reversible hydrogen electrode, RHE) under AM 1.5 irradiation, which was the highest current obtained so far using undoped α-Fe_2O_3 films from electrodeposition. When further decorated with Co-Pi co-catalyst, the optimized Co-Pi/α-Fe_2O_3 photoanode showed incident photon-to-current conversion efficiencies (IPCE) higher than 18% at 400 nm with a stable photocurrent of ~1.89 mA cm^{-2}. The as-prepared α-Fe_2O_3 film also showed excellent stability and degradation efficiency (rate constant ~0.9372 h^{-1}) for PEC degradation of MB in neutral aqueous solution under a positive bias potential.

1. Introduction

The extensive use of cheap and plentiful energy in the form of fossil fuels has brought tremendous revolutions in both human life and nature world. However, the fossil fuels cannot last forever, and the environment has already been and is still being impacted by the burning of fossil fuels. In order to reduce fossil fuel consumption and address the pressing environmental problems, the idea of improving the utilization of clean energy, such as solar energy, has been widely recognized. It is inspiring enough that a photoelectrocatlytic (PEC) technique has been developed to solve these problems by using solar light to drive water splitting and/or organic pollutant degradation since the pioneering work reported by Fujishima and Honda.[1-3]

School of Environmental Science and Engineering, Shanghai Jiao Tong University, No. 800 Dongchuan Rd, Shanghai 200240 PR China. E-mail: zhoubaoxue@sjtu.edu.cn; Fax: (+86)21-54747351

† Electronic supplementary information (ESI) available. See DOI: xxxxx

To date, many efforts have been devoted to developing ideal photoelectrode, which is the key of the PEC technique for converting solar energy to chemical energy, such as PEC water splitting and waste water treatment.[4-9] Among various intensively studied semiconductor materials (e.g. TiO_2, ZnO, WO_3),[10-14] hematite (α-Fe_2O_3) is considered as one of the promising materials in this category, because of its small band gap (~2.1 eV) that enables it to harvest around 40% of the solar spectrum (up to ~600 nm wavelength), excellent stability under alkaline conditions, environmentally benign characteristics, natural abundance, and low cost.[15-19] However, the PEC activity of α-Fe_2O_3 is limited by several factors, including the short lifetime of photogenerated charge carriers (<10 ps), short hole diffusion length (~2-4 nm), and a poor oxygen evolution reaction kinetics.[20-24] To address these limitations, a number of strategies have been developed to improve the PEC properties of α-Fe_2O_3: modifying electronic structure via elemental doping,[25-27] synthesizing nanostructured α-Fe_2O_3 (shorten the pathway that photoexcited electrons/holes have to travel),[28,29] integrating α-Fe_2O_3-based composite photoanode with better conducting material,[30,31] and decorating the surface of α-Fe_2O_3 with co-catalyst, such as cobalt phosphate (Co-Pi), to facilitate oxygen evolution reaction (OER).[32,33]

Numerous methods have been reported for preparing α-Fe_2O_3 photoanode, including hydrothermal,[34,35] spray pyrolysis,[36,37] DC magnetron sputtering,[38] electrodeposition,[25,28,39] atmospheric pressure chemical vapor deposition (APCVD),[33,40] atomic layer deposition (ALD),[41] and anodization.[42] Among these methods, electrodeposition is a facile and cost-effective method for the α-Fe_2O_3 film preparation.

The reported electrodeposition method for preparing α-Fe_2O_3 films includes the following two steps: first, the electrodeposition of FeOOH films; and second, the calcination of it. This method is divided into cathodic electrodeposition and anodic electrodeposition based on the difference of the electrolyte. The cathodic electrodeposition includes the electrochemical reduction of H_2O_2 in order to form OH^- in a solution containing Fe^{3+} and subsequently the precipitation of Fe^{3+} to form FeOOH films near the cathode.[25,39] The Fe^{3+} ions can be precipitated as a result of the increased local pH near the cathode to facilitate the formation of FeOOH films. The anodic electrodeposition, on the other hand, involves the oxidation of Fe^{2+} to Fe^{3+} and the following precipitation of Fe^{3+} for the development of FeOOH films near the anode.[28] The prepared FeOOH films can be converted to α-Fe_2O_3 films by calcination. In sum, the processes for FeOOH films formation in both the cathodic electrodeposition and the anodic electrodeposition are realized from the direct transformation of Fe^{2+} or Fe^{3+} to FeOOH films, which includes the reduction of H_2O_2 to form OH^-, the oxidization of Fe^{2+} to form Fe^{3+}, the precipitation of Fe^{3+} to form FeOOH, the annealing of the FeOOH film to form the α-Fe_2O_3 film, and so on. In this complicated process, various complex compounds of Fe^{2+} and Fe^{3+} in aqueous solution, such as polyhydroxy compounds, polynuclear complex, and Bridging ligand compounds[43-46] would form near the working electrode, causing unavoidable microstructured defects in the as-deposited FeOOH film, which would further be introduced into the final α-Fe_2O_3 structure.[47] Therefore, both cathodic electrodeposition and anodic electrodeposition can hardly produce orderly arranged FeOOH films.

Several works reported the preparation of α-Fe_2O_3 films via direct thermal oxidation of Fe foils, which is an in-situ, simple and promising way to prepare α-Fe_2O_3 photoelectrode.[48-51] Different iron oxide structures can be directly formed on the Fe foils under different annealing conditions and this simple air oxidation of iron can provide a short path to form hematite nanowires.[50] However, the thickness and crystallinity of the oxide film could be difficult to control due to the rapid oxidation of metal Fe during thermal oxidation of the Fe foil. Furthermore, the presence of FeO and/or Fe_3O_4 at the interface of metallic Fe and Fe_2O_3 could be unavoidable. As a result, the photoresponse of the prepared α-Fe_2O_3 photoelectrode is quite poor.

Based on the above discussion, we propose a novel method to prepare α-Fe_2O_3 films, which combines the virtues of both electrodeposition and thermal oxidation while avoids their defects. Specifically, the α-Fe_2O_3 film was obtained via direct electrodeposition of Fe films on the conductive substrate, such as F-doping tin oxide (FTO) coated glass, in alkalescent conditions by adding superfluous ammonia in ferrous sulfate solution, and followed by in-situ thermal oxidation of Fe films to create α-Fe_2O_3 films. This method has several advantages: i) it ensures the uniformity of the deposited Fe film and the resulted α-Fe_2O_3 film as the alkalescent condition should prevent the corrosion of the as-deposited Fe; ii) it should facilitate the deposition of the Fe film in an orderly arrangement since the existence of ferrous hydroxide compounds keeps the reduction rate of Fe^{2+} to Fe moderately, which prevents the generation of microstructured defects in the deposited film, distinguishing it from the traditional strategies such as the direct electrodeposition of FeOOH films from Fe^{2+} or Fe^{3+}; iii) it prevents the presence of undesired phases of FeO and/or Fe_3O_4 appearing in the traditional thermal oxidation of Fe foils because the uniform and tunable Fe film on the FTO substrate can be transformed into α-Fe_2O_3 completely; iv) it facilitates the generation and transport/collection of photo-generated charges in the as-prepared α-Fe_2O_3 film for its tunable thickness, pure phase and lesser microstructured defects.

In this work, the feasibility of using the above described facile method to prepare highly photoactive α-Fe_2O_3 films for efficient PEC water splitting and organic pollutant degradation has been investigated. The result indicates that the as-deposited Fe film can be completely converted into α-Fe_2O_3, and the thickness and the crystallinity of the α-Fe_2O_3 film are tunable via adjusting the deposition durations of the Fe film and annealing conditions, respectively. The effects of annealing temperature and annealing time on PEC water splitting performance of α-Fe_2O_3 films were observed, respectively. Co-Pi decorated α-Fe_2O_3 films were also prepared via photo-assisted electrodeposition to increase the oxygen evolution reaction efficiency at a decreased over-potential. Finally, the effect of PEC organic pollutant degradation with the α-Fe_2O_3 films was examined.

2. Experimental

2.1. Synthesis of α-Fe_2O_3 Film

The Fe film was first electrodeposited on the F-doping tin oxide (FTO) coated glass substrate (13 Ωcm^{-1}) in a two-electrode configuration with the FTO glass working as cathode and a platinum foil as anode (see Fig. 1 and Fig. S1†). The distance between the cathode and the anode was ~3 cm. The electrolyte was prepared by dissolving 5 g $FeSO_4 \cdot 7H_2O$ and 30 mL ammonia (27%) in 150 mL deionized water (the tested pH=10.8 at 25 ºC). The electrodeposition was carried out at 2 V for 15, 30, 45 and 60 s with a vigorous stirring. The as-deposited Fe film was rinsed with deionized water for 5 min and then dried at 50 ºC with a gentle stream of nitrogen gas for 1 h, which was followed by thermal oxidation in air.

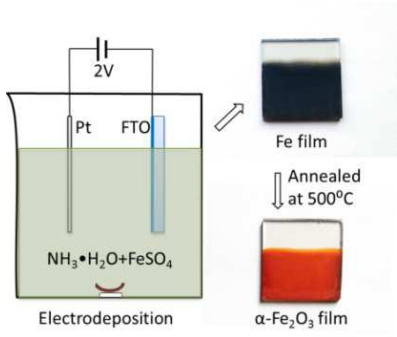

Fig. 1 A scheme showing the electrodeposition process and the as prepared Fe film and the α-Fe_2O_3 film (deposited for 10 min).

Deposition of Co-Pi on the surface of the as-prepared α-Fe_2O_3 film was carried out in a three-electrode system with the α-Fe_2O_3 film used as the working electrode, a platinum foil as the counter electrode and a saturated calomel electrode (SCE) as the reference via photo-assisted electrodeposition (PED) method. 0.1 M sodium phosphate buffer solution at pH 7 containing 5 mM $Co(NO_3)_2$ was used as an electrolyte. The PED was carried out at 0.1 V under the illumination of 1 sun-simulated solar light. After PED, the α-Fe_2O_3 film modified with Co-Pi was rinsed with deionized water for 5 min and then dried at 50 ºC for 1 h.

2.2. Characterization

The morphologies and microstructures of the samples were investigated by FE-SEM (Sirion200, Philips, Netherlands) equipped with an energy dispersive X-ray detector (EDX). XPS spectra were measured with an AXIS Ultra DLD (Kratos, Shimadzu) using non-chromatic Al K_α radiation at 12 kV and 25 mA. The crystal phase of the samples was characterized with X-ray diffractometry (XRD) (AXS-8 Advance, Bruker, Germany). Raman spectra were recorded on SENTERRA R200 system (Bruker, Germany) with laser excitation of 532 nm. UV−visible absorption spectra of the samples were recorded on a UV−Vis photospectrometer (TU-1901, Pgeneral, China).

2.3. Photoelectrocatalytic Measurements

The photoelectrocatalytic (PEC) water splitting experiments were carried out in 1 M KOH electrolyte using a three-electrode system with an SCE as the reference, a platinum foil as the auxiliary electrode, and as-prepared films as the working electrode. The PEC tests were controlled by an electrochemical workstation (CHI 660c, CH Instruments Inc., USA). A 350 W Xe lamp (Shanghai Hualun Bulb Factory) with AM 1.5 filter was used for light illumination (light density: 100 mW cm^{-2}). Incident-photon-to-charge conversion efficiency (IPCE) was measured by a system comprising a monochromator (Zolix, China), a 500 W xenon arc lamp, a calibrated silicon photodetector, and a power meter.

The PEC degradation of Methylene Blue (MB) experiment was conducted under the following conditions: AM 1.5 irradiation, vigorous stirring, 0.6 V (vs. SCE) of electric bias, pH 7, and 0.01 mol L^{-1} sodium sulfate as supporting electrolyte. The photocatalytic (PC) degradation was performed without applying an external potential on the working electrodes. The initial concentration of MB solution was 5 mg L^{-1} and the reaction solution was 25 mL during the experiment. At different time intervals, the reaction solution was analyzed using a UV–vis spectrophotometer (UV2102 PCS, UNICO, Shanghai).

The IMPS was tested by using an electrochemical workstation (ZENNIUM, ZAHNER-elecktrik GmbH&Co.KG, Germany) equipped with a controlled-intensity-modulated-photospectroscopy setup (CIMPS, PP211, ZAHNER-elecktrik GmbH&Co.KG, Germany) following a three-electrode configuration with the prepared α-Fe_2O_3 film working as the working electrode, a platinum foil as the counter electrode, and an SCE as the reference electrode with a 1 M KOH electrolyte. A white light lamp (WLC02, ZAHNER-elecktrik GmbH&Co.KG, Germany) was used as the light source. The modulated light in the frequency range of 0.1 Hz – 10 KHz superimposed on a steady DC light intensity of 80 mWcm^{-2} was applied. The bias potential applied on the working electrode was 0.23 V *vs.* SCE.

3. Results and Discussion

3.1. Fabrication of α-Fe_2O_3 Film

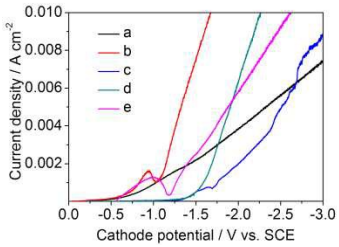

Fig. 2 The voltammetric curves tested in various electrolytes: (a) 5 g $FeSO_4•7H_2O$ dissolved in 180 mL deionized water; (b) 5 g $FeSO_4•7H_2O$ and 2.37 g Na_2SO_4 dissolved in 180 mL deionized water; (c) 5 g $FeSO_4•7H_2O$ dissolved in 180 mL deionized water with the pH adjusted to 10.8 by NaOH; (d) 5 g $FeSO_4•7H_2O$ and 2.75 g Na_2SO_4 dissolved in 180 mL deionized water with the pH adjusted to 10.8 by NaOH; (e) 5 g $FeSO_4•7H_2O$ and 30 mL ammonia (27 %) dissolved in 150 mL deionized water (pH=10.8). Scan rate: 5 mV S^{-1}.

In this work, we have provided an alternative way to prepare Fe films via electrodeposition in ammonia conditions. In order to reveal the effect of ammonia on the electrolyte, various electrolytes have been used for electrodepositing Fe films. The voltammetric curves carried out on FTO substrates in different electrolytes are shown in Fig. 2. As can be seen from Fig. 2, the onset potential increased after the pH was adjusted by NaOH (see curve a *vs.* curve c and curve b *vs.* curve d), and the deposition current increased with the increase of the concentration of electrolyte (see curve a *vs.* curve b and curve c *vs.* curve d). However, a comparison between curve d and curve e reveals that the electrodeposition behavior in the electrolyte with ammonia differed from that in the electrolyte with NaOH even though the pH was the same, suggesting that the reaction occurring on the FTO substrate in the electrolyte with ammonia was different from that in the electrolyte with NaOH. This

speculation is verified by the XRD patterns of the deposited films from the electrolyte with NaOH shown in Fig. S2,† which indicates that the deposited films were tetragonal Sn films. However, the XRD patterns of the as-deposited film from the electrolyte with ammonia shown in Fig. 3(A) indicate that it was cubic Fe film. From the inset paragraph in Fig. 1, this Fe film showed good uniformity with a matte black color, and was well adherent to the substrate. Thus, the ammonia condition leads to a significant enhancement of the uniformity of the as-deposited Fe film and prevents the reduction of SnO_2 in strong alkaline (NaOH) condition. (Detailed discussion seen ESI†)

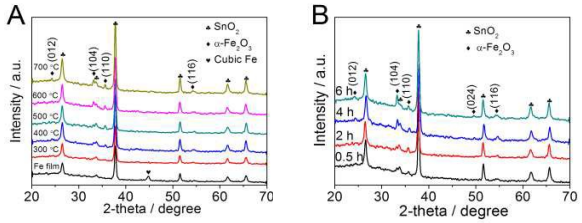

Fig. 3 XRD patterns of α-Fe_2O_3 film (deposited for 30 s) annealed at (A) different temperatures for 2 h, (B) 500 °C for various durations.

The as-deposited Fe films were annealed in the air at different temperatures for different durations, and their XRD patterns are shown in Fig. 3. Fig. 3(A) shows the XRD patterns of Fe film annealed at different temperatures ranging from 300 to 700 ºC for 2 h. It can be seen that the as-deposited Fe film with cubic phase changed to amorphous phase at 300 ºC and the characteristic peaks of α-Fe_2O_3 (JCPDS no.890598) appeared at 400 ºC. When annealed at 500 ºC, the intensity of (110) peak became the strongest among the samples. With the annealing temperature further increased, the intensity of (104) peak increased at 600 ºC, and (012) peak appeared at 700 ºC.

Fig. 3(B) gives the XRD patterns of Fe film annealed at 500 ºC for different durations. (110) peak of hematite structure appeared after being annealed for 0.5 h and it was intensified with a longer annealing time of 2 h. With longer annealing time, a new (012) peak appeared and the intensity of the (104) peak was obviously enhanced. In contrast, there was no significant change for the (110) peak. It is noted that (110) peak first appeared during annealing, applying that α-Fe_2O_3 film has a preferred orientation in the [110] direction. It is a favorable result because the conductivity of α-Fe_2O_3 along the [110] direction is 4 orders of magnitude higher than that in the orthogonal direction.[40]

In order to further obtain physicochemical characteristics, Raman and XPS tests were performed on a representative α-Fe_2O_3 film (deposited for 30 s, annealed at 500 ºC for 2 h). Raman spectra shown in Fig. 4(A) exhibit the characteristic peaks of α-Fe_2O_3 at 212, 271, 384, 484, 579, and 1282 cm^{-1}.[52] Unlike some previous reports,[36,53] the peak located at approximately 650 cm^{-1}, which is assigned to magnetite (Fe_3O_4) or a disordered phase (possibly induced by the presence of FeO), is almost negligible, indicating that the as-prepared film was high purity with α-Fe_2O_3. The XPS spectra of the α-Fe_2O_3 film shown in Fig. 4(B) indicate the existence of iron (Fe), oxygen (O) and carbon (C). The existence of C could be attributed to an impurity introduced during sample preparation or absorption of CO_2 from air. Fig. 4(C) shows the Fe 2p core-level spectra, which exhibited a Fe $2p_{3/2}$ line at a binding energy of 710.8 eV and a Fe $2p_{1/2}$ line at a binding energy of 724.1 eV. The binding energy of Fe $2p_{3/2}$ line is a typical XPS value from α-Fe_2O_3, which is distinct from the values from Fe_3O_4 (~709 eV) and FeO (709.1–709.5 eV).[15,54] A characteristic satellite peak of α-Fe_2O_3 also appeared at 718.8 eV.[50] In general, these results confirmed that a-Fe_2O_3 thin films can be synthesized with a pure phase via a route including electrodepotion of Fe film in electrolyte with ammonia and the following in-situ thermal oxidation in air.

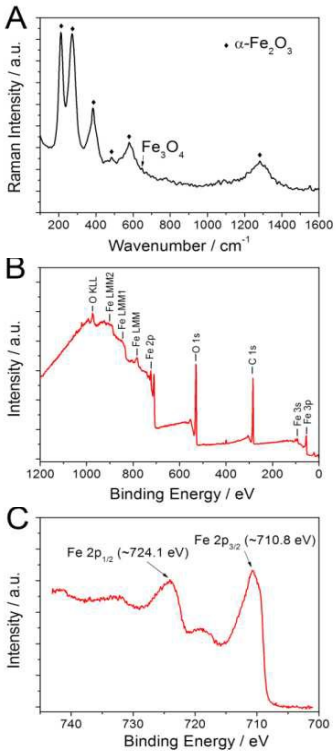

Fig. 4 (A) Raman spectra, (B) XPS survey data, and (C) Fe 2p core-level spectra of α-Fe_2O_3 film (deposited for 30 s, annealed at 500 °C for 2 h).

The typical SEM image of the as-deposited Fe film is shown in Fig. S3.† As we can see, the Fe film consists of nanoparticles, and the surface is relatively smooth. Fig. 5 shows the SEM micrographs of α-Fe_2O_3 films (500 °C for 2 h) from Fe films obtained with different deposition times. Fig. 6 shows the corresponding cross-section SEM images. After annealed in the air, the nanoparticle-like Fe films were transformed into compact α-Fe_2O_3 films, especially for the sample with 5 min deposition (Fig. 5(A)). The α-Fe_2O_3 film of the samples deposited for 30 s, 45 s and 60 s appeared a similar surface morphology showing a compact film with some nanoparticles on the surface (Fig. 5(B)-(D)). All the as-prepared α-Fe_2O_3 films were well adherent to the FTO substrate, and the

thickness of the film was linear dependence with the deposition time (Fig. 6 and Fig. S4†).

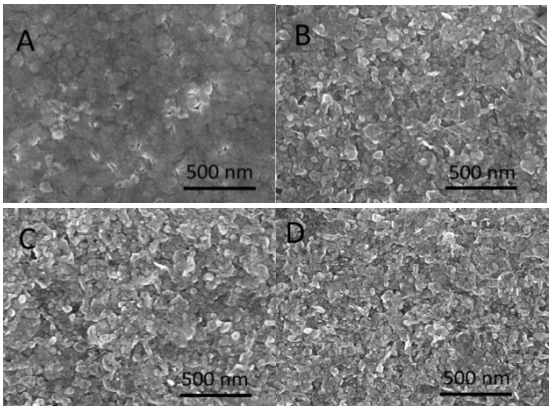

Fig. 5 Surface SEM images of α-Fe_2O_3 films deposited for (A) 15 s, (B) 30 s, (C) 45 s, and (D) 60 s. All presented films were oxidized in air at 500 °C for 2 h.

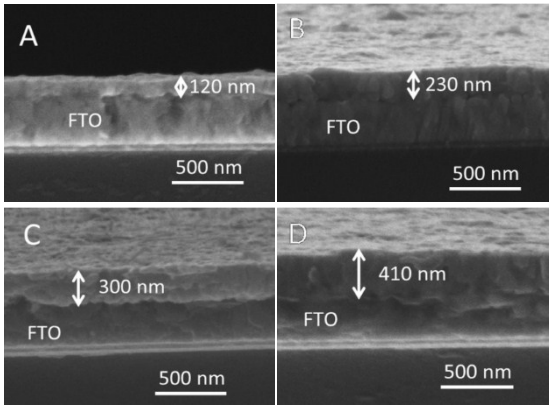

Fig. 6 Cross-section SEM images of α-Fe_2O_3 films deposited for (A) 15 s, (B) 30 s, (C) 45 s, and (D) 60 s. All presented films were oxidized in air at 500 °C for 2 h.

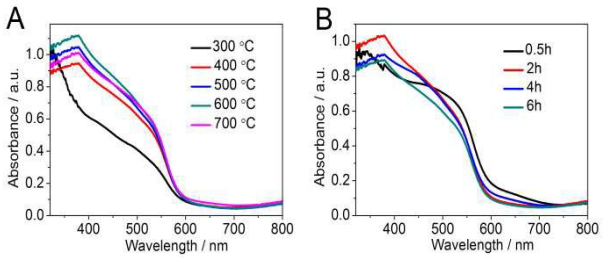

Fig. 7 UV-Vis absorption spectra of α-Fe_2O_3 film (deposited for 30 s) annealed at (A) different temperatures for 2 h, (B) 500 °C for various durations.

α-Fe_2O_3 is an n-type semiconductor with a band gap of ~ 2.1 eV which means that it can absorb the light with a wavelength under 590 nm. This is verified by the UV-Vis absorption spectra of α-Fe_2O_3 films shown in Fig. 7. With the increase of the annealing temperature from 400 to 600 °C, the absorption intensity was gradually increased until at 700 °C, where the intensity was decreased instead in the region of 320-500 nm and lower than that of the sample annealed at 500 °C (Fig. 7(A)). When annealed at 500 °C for 0.5 h, the absorption intensity in the region of 320-480 nm was weaker than that of the sample annealed for 2 h, whereas it was stronger in the region of 480-720 nm (Fig. 7(B)). As the annealing time was increased to 4 h, the absorption intensity was decreased in the region of 320-450 nm compared with that of the sample annealed for 2 h. With the annealing time further increased to 6 h, the absorption intensity was further decreased in the region of 320-550 nm compared with that of the sample annealed for 4 h. According to the XRD patterns shown in Fig. 3, it can be concluded that a stronger (110) peak of α-Fe_2O_3 would enhance the absorption intensity in the response region, and the (104) peak would further increase the absorption intensity until the appearance of (012) peak. After that, the absorption intensity would decrease with the increase of (104) peak intensity. This result indicates that the light absorption intensity of α-Fe_2O_3 film is related to the crystallinity and lattice orientation of the film.

3.2. Photoelectrocatalytic characterization

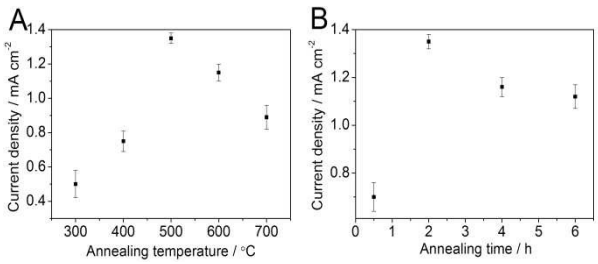

Fig. 8 Photocurrent density of α-Fe_2O_3 film (deposited for 30 s) annealed at (A) different temperatures for 2 h, (B) 500 °C for various durations, measured at 1.23 V *vs.* RHE in the 1 M KOH electrolyte under AM 1.5 illumination.

The PEC water splitting activity of the α-Fe_2O_3 films was studied in a three-electrode PEC cell to observe their PEC water oxidation response in 1 M KOH under simulated solar light irradiation (100 $mWcm^{-2}$, AM 1.5). The potentials were measured relative to the saturated calomel electrode (SCE) reference electrode and converted to the reversible hydrogen electrode (RHE) scale according to the following equation:

$$E_{RHE} = E_{SCE} + 0.0591 \times pH + E^{0}_{SCE},$$

where the E_{RHE} is the calculated potential *versus* RHE, E_{SCE} is the measured potential, pH is about 13.9 and E^{0}_{SCE} is about 0.2415 V at 25 ºC. The photocurrent densities measured at 1.23 V *vs.* RHE of the α-Fe_2O_3 films annealed at different temperatures for 2 h are shown in Fig. 8 (A). The α-Fe_2O_3 film annealed at 500 ºC showed the highest photocurrent density of ~1.35 mA cm^{-2}, while the Fe_2O_3 film annealed at 300 ºC showed the lowest photocurrent, possibly because the insufficient crystallization of the film leads to a higher defect density and lower conductivity. The α-Fe_2O_3 film annealed at 600 ºC showed a smaller photocurrent than that of the sample annealed at 500 ºC, which should be attributed to the rapid increase of resistance of the FTO film (see Fig. S5).† The increased resistance can also explain the decrease of photocurrent of the sample annealed at 700 ºC. Moreover, the decreased absorption intensity in the region of 320-500 nm of the sample annealed at 700 ºC should also account for the

decrease of photocurrent. Fig. 8(B) shows the photocurrent densities of α-Fe_2O_3 films annealed at 500 ºC for different times. The sample annealed for 0.5 h showed the lowest photocurrent of ~0.8 mA cm^{-2}, while the highest photocurrent of ~1.35 mA cm^{-2} was obtained for the sample annealed for 2 h. When the annealing time was further increased, the photocurrent decreased slightly. According to the XRD patterns (Fig. 3) and the UV-Vis absorption spectra (Fig. 7), the α-Fe_2O_3 film showing the strongest (110) peak in the XRD patterns could have marvelously improved photocurrent density (the α-Fe_2O_3 films annealed at 500 ºC for 2 h *vs.* 400 ºC for 2 h or 500 ºC for 0.5 h). However, the sample with the (012) peak showed relatively small photocurrent density (the α-Fe_2O_3 films annealed at 500 ºC for 4 h or 6 h, or 700 ºC for 2 h). This interesting result should be due to the superior conductivity of α-Fe_2O_3 along the [110] direction compared with that in the orthogonal direction mentioned above.

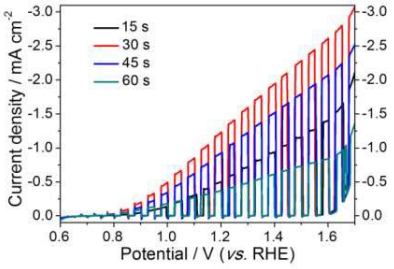

Fig. 9 Photocurrent-potential (*I-V*) curves with chopped light for PEC water oxidation reaction of the α-Fe_2O_3 films deposited for different durations (annealed at 500 °C for 2 h) measured in the 1 M KOH electrolyte under AM 1.5 illumination.

Fig. 9 shows the chopped photocurrent-potential (*I-V*) curves of the α-Fe_2O_3 films with different deposition times (annealed at 500 °C for 2 h). Obviously, the sample with a deposition time of 30 s showed the highest photocurrent response among the four tested samples. However, further increase of the deposition time reduced the PEC water oxidation performance. For example, the sample 60 s showed the lowest photocurrent response. As aforementioned, α-Fe_2O_3 is an indirect band gap semiconductor with a very short lifetime of photogenerated charge carriers (<10 ps) and short hole diffusion length (~2-4 nm).[24] Although the increase of film thickness would improve the light absorption for generating more photocharges, it would also increase the recombination rate of photogenerated electron-hole pairs and decrease the efficiency of charge transfer. It means that the benefit from enhanced light absorption could be offset by rapidly increasing recombination rate, especially in the excessively thick film. Hence, a suitable thickness of α-Fe_2O_3 film would be crucial for both light absorption and charge transfer in PEC application. In this work, the optimum sample (30s) contains an α-Fe_2O_3 film with a thickness of ~230 nm (Fig. S4).†

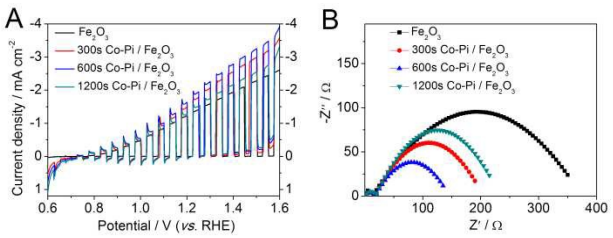

Fig. 10 (A) Photocurrent-potential (I-V) curves with chopped light for PEC water oxidation reaction of the Co–Pi/α-Fe2O3 films with different photo-assisted electrodeposition times; (B) Nyquist plots of the Co-Pi/α-Fe2O3 photoanodes under 1.23 V vs. RHE. The measurements were done in the 1 M KOH electrolyte under AM 1.5 illumination.

Cobalt–phosphate (Co–Pi) is an efficient surface water-oxidation co-catalyst that can improve the water oxidation kinetics on the photoanode surface in PEC water splitting.[33,56,57] So, in order to improve the performance of the prepared α-Fe_2O_3 film in PEC water splitting, Co–Pi decorated α-Fe_2O_3 films (Co–Pi/α-Fe_2O_3) with different photo-assisted electrodeposition (PED) times were prepared. The EDX result of the prepared 600 s Co–Pi/α-Fe_2O_3 film (600 s represents the deposition time of Co-Pi) shown in Fig. S6† indicates that Co-Pi was decorated on the α-Fe_2O_3 film uniformly. The *I-V* curves of the Co–Pi/α-Fe_2O_3 films with different PED times are shown in Fig. 10(A). As can be seen from Fig. 10(A), the decoration of Co–Pi on the α-Fe_2O_3 film could reduce the onset potential of the photoanode for water splitting under both light illumination and dark, which means Co–Pi can facilitate the water oxide reaction taking place at Fe_2O_3||electrolyte. With deposition of Co–Pi for 300 s, the photocurrent response of the sample increased remarkably from ~1.35 mA cm^{-2} to ~1.72 mA cm^{-2} at 1.23 V *vs.* RHE. With the PED time further increased to 600 s, the photocurrent response increased slightly with a photocurrent of ~1.89 mA cm^{-2}. However, the photocurrent response fell to ~1.53 mA cm^{-2} after 1200 s PED. As can be seen from the Nyquist plots of these samples shown in Fig. 10(B), Co–Pi could decrease the resistance of the α-Fe_2O_3 films in PEC water splitting, and 600 s Co–Pi/α-Fe_2O_3 photoanode showed the lowest resistance. However, a thicker Co–Pi layer, such as 1200 s Co–Pi/α-Fe_2O_3, would increase the resistance in the Co–Pi layer itself and finally reduce the charge transfer properties. Therefore, 600 s is the optimum time for deposition of Co-Pi on the α-Fe_2O_3 film in this case.

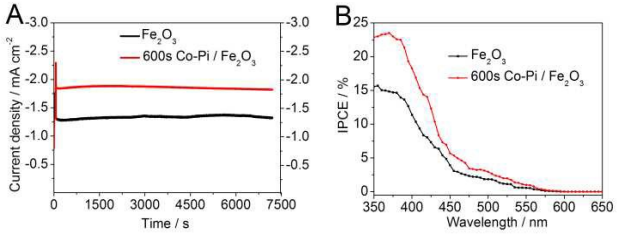

Fig. 11 (A) The photocurrent-time curves and (B) IPCE plots of α-Fe_2O_3 photoanode and 600s Co–Pi/α-Fe_2O_3 photoanode measured at 1.23 V *vs.* RHE in the 1 M KOH electrolyte.

The stability of the prepared photoanode in PEC water splitting is crucial for both fundamental and practical studies. Fig. 11(A) shows the photocurrent curves of optimized α-Fe_2O_3 photoanode and Co–Pi/α-Fe_2O_3 photoanode measured at 1.23 V *vs*. RHE in the 1 M KOH electrolyte under AM 1.5 illumination for 2 h. The photocurrent of α-Fe_2O_3 photoanode and 600 s Co–Pi/α-Fe_2O_3 photoanode were ~1.34 mA cm^{-2} and ~1.85 mA cm^{-2}, respectively, without any significant decline, indicating that both photoanodes exhibited excellent stability in PEC water splitting. To quantitatively investigate the photoactivity of the α-Fe_2O_3 films as a function of wavelength, Incident-photon-to-charge conversion efficiency (IPCE) measurements were performed on the optimized α-Fe_2O_3 photoanode and Co–Pi/α-Fe_2O_3 photoanode at 1.23 V vs RHE, and the result is shown in Fig. 11(B). The IPCE behaviors of both photoanodes were observed between 350 and 570 nm, which is roughly consistent with the light absorption spectrum of α-Fe_2O_3 film (see Fig. 7). This indicates that the absorbed photons with different energies have been converted to photocurrents successfully. The IPCE values of Co–Pi/α-Fe_2O_3 photoanode were higher than those of the bare α-Fe_2O_3 photoanode in the full response region, which means that the decoration of Co-Pi co-catalyst could make the absorbed photons with different energies convert to current more efficiently. The IPCE values in the short wavelength region (<380 nm) were up to ~22% for Co–Pi/α-Fe_2O_3 photoanode, much higher than those of the reported α-Fe_2O_3 film prepared via anodic or cathodic electrodeposition. Furthermore, it should be noted that it is a common characteristic of α-Fe_2O_3 photoanode that the IPCE curve has a more rapid decrease over 380-450 nm compared with the absorption spectrum (see Fig. 7). This is because the photons in this region only excite indirect d→d transition of Fe^{3+}, which only generates electron-hole pairs localized in Fe^{3+} and cannot provide effective energy for water oxidation.[23,58,59]

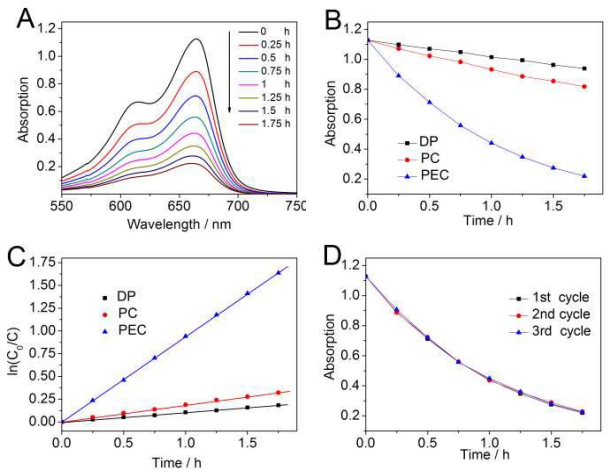

Fig. 12 (A) UV–vis absorption spectra of MB solution during different stages (at 15 min interval) of PEC reaction by α-Fe_2O_3 film; (B) The PEC (at a bias potential of 0.6 V vs. SCE), PC and direct photolysis (DP) of MB solutions; (C) The PEC, PC and DP kinetic curves of MB; (D) variation of the MB concentration in PEC degradation by α-Fe_2O_3 film in three PEC cycles.

The PEC activity of the optimized α-Fe_2O_3 film was also investigated by organic compound degradation experiments. The PEC (at a bias potential of 0.6 V vs. SCE), photocatalytic (PC, PEC without bias potential), and direct photolytic (DP) degradation of MB in neutral aqueous solutions were performed under given conditions, respectively. Fig. 12(A) shows the UV−vis absorption spectra of MB solution after PEC reaction by the α-Fe_2O_3 film for different times. The characteristic peak of MB (at 665 nm) was found decreasing steadily with the reaction time. As shown in Fig. 12(B), the performance of the α-Fe_2O_3 film in different systems follows the tendency of PEC > PC > DP. The highest rate constant was ~0.9372 h^{-1} obtained by PEC, which is 5.06 and 9.12 times higher than that of PC (~0.1851 h^{-1}) and DP (~0.1028 h^{-1}), respectively. This result suggests that the presence of α-Fe_2O_3 film can improve the degradation efficiency of MB, especially under a positive bias for enhanced separation of photogenerated electron-hole pairs in the α-Fe_2O_3 film. Since the kinetic constant of PC reaction is only 1.8 times higher than that of DP reaction, it also indicates the poor transport property of photogenerated charges in the α-Fe_2O_3 film without a positive bias. The reusing test of the α-Fe_2O_3 film for PEC degradation of MB in three PEC cycles shown in Fig. 12(D) further indicates that the as-prepared α-Fe_2O_3 film is stable for PEC applications, such as organic compound degradation.

3.3. IMPS measurements

In order to illustrate the lesser microstructured defects in the α-Fe_2O_3 films prepared in this work, intensity modulated photocurrent spectroscopy (IMPS) has been applied to measure the charge carrier transit times (τ_d) in the α-Fe_2O_3 films prepared in this work and the anodic α-Fe_2O_3 films prepared via traditional anodic electrodeposition[28]. IMPS is a powerful, non-destructive characterization technique for analyzing the photo-generated carriers transportion and recombination/relaxation information in the photoelectrode.[60-62] The average time of photogenerated charges need to reach the back contact, the transit time τ_d, can be estimated from $\tau_d = (2\pi \bullet f_{min}(\mathrm{IMPS}))^{-1}$, where f_{min} is the frequency at the minimal value in the IMPS plot.[60] The transit time reflects the recombination probability of photogenerated electrons and holes in the photoeletrode, which is always related to the microstructure properties of the photoeletrode film.[62]

The XRD patterns shown in Fig. S8† indicate that the annealed film consisted of α-Fe_2O_3, the same with what has been reported in the literature.[28] The SEM images shown in Fig. S9† indicate that the as-deposited FeOOH film and the anodic α-Fe_2O_3 film were uniform, and the thickness of the anodic α-Fe_2O_3 film was ~410 nm. For comparison, the α-Fe_2O_3 film with a deposition time of 60 s whose thickness was also ~410 nm (Fig. S4†) was selected for the IMPS test and this film was denoted as 60s/α-Fe_2O_3 film.

Fig. 13 shows the IMPS plots of the anodic α-Fe_2O_3 film and the 60s/α-Fe_2O_3 film. According to the f_{min}, the calculated τ_d values of the anodic α-Fe_2O_3 film and the 60s/α-Fe_2O_3 film are 3.004 ms and 1.197 ms, respectively. The transit time τ_d of the

anodic α-Fe_2O_3 film is nearly three-fold that of the 60s/α-Fe_2O_3 film. This result demonstrates that the photogenerated charges transport easily to reach the back contact in the 60s/α-Fe_2O_3 film when compared with the anodic α-Fe_2O_3 film. Since the nanostructured defects in the photoelectrode film can generate a lot of crystal boundaries which will impede the transportion of charges and promote the recombination of photogenerated electron/hole,[62] the IMPS reslut indicates that the α-Fe_2O_3 film prepared in this work should possess lesser nanostructured defects when compared with the anodic α-Fe_2O_3 film prepared via traditional electrodeposition method.

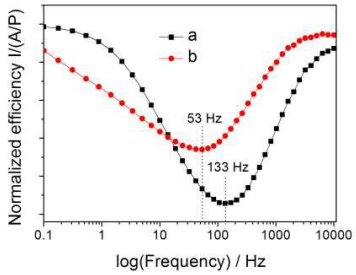

Fig. 13 The IMPS plots of the (a) anodic α-Fe_2O_3 film and (b) 60s/α-Fe_2O_3 film.

4. Conclusion

In summary, a facile method for preparing photocorrosion stable and highly photoactive α-Fe_2O_3 films has been proposed in this work. The ammonia contained in the electrolyte is crucial to preparing the uniform Fe film via an electrodeposition method. The Fe film can be transformed into α-Fe_2O_3 film completely via in-situ thermal oxidation. The optimized α-Fe_2O_3 photoanode showed a stable PEC water oxidation current of ~1.35 mA cm^{-2} at 1.23 V *vs.* RHE under AM 1.5 irradiation. After decorated with Co-Pi co-catalyst, the optimized Co-Pi/α-Fe_2O_3 photoanode showed IPCE higher than 18% at 400 nm with a stable photocurrent of ~1.89 mA cm^{-2} for the PEC water splitting. The α-Fe_2O_3 photoanode also showed excellent stability and degradation efficiency (rate constant ~0.9372 h^{-1}) for PEC degradation of MB in neutral aqueous solution. This paper provides a useful insight into the design and fabrication of α-Fe_2O_3 photoanode for potentially cost-effective and highly-efficient PEC applications.

Acknowledgements

The authors would like to acknowledge the National Nature Science Foundation of China (Nos. 21276153, 21177085, 21207088), the Doctoral Program of the Ministry of Education of China (No. 20110073110029), and the Shanghai Basic Research Key Project (11JC1406200) and Shanghai Yangfan Program (14YF1401500) for financial support.

References

1 A. Fujishima and K. Honda, *Nature*, 1972, **238**, 37–38.
2 C.-C. Wang, J.-R. Li, X.-L. Lv, Y.-Q. Zhang and G. Guo, *Energy Environ. Sci.*, 2014, **7**, 2831-2867.
3 T. Lin, C. Yang, Z. Wang, H. Yin, X. Lü, F. Huang, J. Lin, X. Xie and M. Jiang, *Energy Environ. Sci.*, 2014, **7**, 967-972.
4 D. Wang, X. Zhang, P. Sun, S. Lu, L. Wang, C. Wang, Y. Liu, *Electrochim. Acta*, 2014, **130**, 290–295.
5 Q. Zeng, J. Bai, J. Li, Y. Li, X. Li, and B. Zhou, *Nano Energy*, 2014, **9**, 152–160.
6 Q. Chen, J. Li, X. Li, K. Huang, B. Zhou, and W. Shangguan, *ChemSusChem*, 2013, **6**, 1276–1281.
7 D. Wang, X. Zhang, P. Sun, S. Lu, L. Wang, Y. Wei, Y. Liu, *Int. J. Hydrogen Energy*, 2014, **39**, 16212–16219.
8 Q. Zheng, B. Zhou, J. Bai, L. Li, Z. Jin, J. Zhang, J. Li, Y. Liu, W. Cai, and X. Zhu, *Adv. Mater.*, 2008, **20**, 1044–1049.
9 X. Chen, L. Liu, P. Y. Yu and S. S. Mao, *Science*, 2011, **331**, 746–750.
10 J. Bai and B. Zhou, *Chem. Rev.*, 2014, **114**, 10131–10176.
11 B. Liu, A. Khare and E. S. Aydil, *Chem. Commun.*, 2012, **48**, 8565-8567.
12 X. Chen, S. Shen, L. Guo and S. S. Mao, *Chem. Rev.*, 2010, **110**, 6503–6570.
13 J. Su, X. Feng, J. D. Sloppy, L. Guo, and C. A. Grimes, *Nano Lett.*, 2011, **11**, 203–208.
14 B. Liu and E. S. Aydil, *Chem. Commun.*, 2011, **47**, 9507-9509.
15 G. Wang, Y. Ling, D. A. Wheeler, K. E. N. George, K. Horsley, C. Heske, J. Z. Zhang, and Y. Li, *Nano Lett.*, 2011, **11**, 3503–3509.
16 H. Dotan, K. Sivula, M. Grätzel, A. Rothschild and S. C. Warren, *Energy Environ. Sci.*, 2011, **4**, 958-964.
17 D. A. Wheeler, G. Wang, Y. Ling, Y. Li and J. Z. Zhang, *Energy Environ. Sci.*, 2012, **5**, 6682–6702.
18 L. Zhou, H. Xu, H. Zhang, J. Yang, S. B. Hartono, K. Qian, J. Zou and C. Yu, *Chem. Commun.*, 2013, **49**, 8695–8697.
19 H. Zhang, L. Zhou and C. Yu, *RSC Adv.*, 2014, **4**, 495–499.
20 F. L. Formal, S. R. Pendlebury, M. Cornuz, S. D. Tilley, M. Grätzel and J. R. Durrant, *J. Am. Chem. Soc.*, 2014, **136**, 2564–2574.
21 S. R Pendlebury, X. Wang, F. L. Formal, M. Cornuz, A. Kafizas, S. D. Tilley, M. Grätzel and J. R. Durrant, *J. Am. Chem. Soc.*, 2014, **136**, 9854–9857.
22 Z. Huang, Y. Lin, X. Xiang, W. Rodríguez-Córdoba, K. J. McDonald, K. S. Hagen, K. Choi, B. S. Brunschwig, D. G. Musaev, C. L. Hill, D. Wang and T. Lian, *Energy Environ. Sci.*, 2012, **5**, 8923–8926.
23 M. Barroso, S. R. Pendlebury, A. J. Cowan and J. R. Durrant, *Chem. Sci.*, 2013, **4**, 2724-2734.
24 S. R. Pendlebury, M. Barroso, A. J. Cowan, K. Sivula, J. Tang, M. Grätzel, D. Klug and J. R. Durrant, *Chem. Commun.*, 2011, **47**, 716-718.
25 Y.-S. Hu, A. Kleiman-Shwarsctein, A. J. Forman, D. Hazen, J.-N. Park and E. W. McFarland, *Chem. Mater.*, 2008, **20**, 3803–3805.
26 D. Cao, W. Luo, J. Feng, X. Zhao, Z. Li and Z. Zou, *Energy Environ. Sci.*, 2014, **7**, 752-759.
27 S. Saremi-Yarahmadi, K. G. Upul Wijayantha, A. A. Tahir and B. Vaidhyanathan, *J. Phys. Chem. C*, 2009, **113**, 4768–4778.
28 R. L. Spray and K.-S. Choi, *Chem. Mater.*, 2009, **21**, 3701–3709.
29 A. Mao, N.-G. Park, G. Y. Han and J. H. Park, *Nanotechnology*, 2011, **22**, 175703.
30 L. Wang, A. Palacios-Padrs, R. Kirchgeorg, A. Tighineanu and P. Schmuki, *ChemSusChem* 2014, **7**, 421–424.

31 T. Jin, P. Diao, Q. Wu, D. Xua, D. Hu, Y. Xie, and M. Zhang, *Appl. Catal. B: Environ.*, 2014, **148-149**, 304– 310.
32 M. W. Kanan, Y. Surendranath and D. G. Nocera, *Chem. Soc. Rev.*, 2009, **38**, 109-114.
33 D. K. Zhong, M. Cornuz, K. Sivula, M. Grätzel and D. R. Gamelin, *Energy Environ. Sci.*, 2011, 4, 1759–1764.
34 L. Vayssieres, N. Beermann, S. Lindquist and A. Hagfeldt, *Chem. Mater.*, 2001, **13**, 233–235.
35 Y. Ling, G. Wang, D. A. Wheeler, J. Z. Zhang and Y. Li, *Nano Lett.*, 2011, **11**, 2119–2125.
36 S. U. M. Khan and J. Akikusa, *J. Phys. Chem. B*, 1999, **103**, 7184–7189.
37 E. Thimsen, F. Le Formal, M. Grätzel and S. C. Warren, *Nano Lett.*, 2011, **11**, 35–43.
38 J. A. Glasscock, P. R. F. Barnes, I. C. Plumb and N. Savvides, *J. Phys. Chem. C*, 2007, **111**, 16477–16488.
39 A. Kleiman-Shwarsctein, Y.-S. Hu, A. J. Forman, G. D. Stucky and E. W. McFarland, *J. Phys. Chem. C*, 2008, **112**, 15900–15907.
40 A. Kay, I. Cesar and M. Grätzel, *J. Am. Chem. Soc.*, 2006, **128**, 15714–15721.
41 Y. Lin, S. Zhou, S. W. Sheehan and Dunwei Wang, *J. Am. Chem. Soc.*, 2011, **133**, 2398–2401.
42 C.-Y. Lee, L. Wang, Y. Kado, M. S. Killian and P. Schmuki, *ChemSusChem*, 2014, **7**, 934–940.
43 A. Dei , D. Gatteschi , L. Pardi , U. Russo, *Inorg. Chem.*, 1991, **30**, 2589–2594.
44 A. A. Kamnev, Y. D. Perfilyev and V. Angelov, *Electrochim. Acta*, 1995, **40**, 1005–1011.
45 S. Li, Z. Chen, Y. Jin, S. Chen, H. Wang, J. Geng, Q. Song, X. Yang, L. Ma, S. Li, Z. Qin and C. Zheng, *Solid State Sci.*, 2011,**13**, 862–866.
46 C. E. Coulombe, J.B. Dixon and L.P. Wilding, *Develop. in Soil Sci.*, 1996, **24**, 115–200.
47 U. Bjoerksten , J. Moser and M. Grätzel, *Chem. Mater*., 1994, **6**, 858–863.
48 L. Wang, C.-Y. Lee, A. Mazare, K. Lee, J. Mller, E.n Spiecker and P. Schmuki, *Chem. Eur. J.*, 2014, **20**, 77–82.
49 B. D Chernomordik, H. B Russell, U. Cvelbar, J. B Jasinski, V. Kumar, T. Deutsch and M. K Sunkara, *Nanotechnology*, 2012, **23**, 194009.
50 S. Grigorescu, C. Lee, K. Lee, S. Albu, I. Paramasivam, I. Demetrescua and P. Schmuki, *Electrochem. Commun.*, 2012, **23**, 59–62.
51 T. Vincent, M. Gross, H. D otan, A. Rothschild, *Int. J. Hydrogen Energy*, 2012, **37**, 8102-8109.
52 D. L. A. de Faria, S. V. Silva and M. T. de Oliveira, *J. Raman Spectrosc.*, 1997, **28**, 873-878.
53 G. Rahman and O. Joo, *J. Mater. Chem. A*, 2013, **1**, 5554–5561.
54 T. Fujii, F. M. F. de Groot and G. A. Sawatzky, *Phys. Rev. B: Solid State*, 1999, **59**, 3195–3202.
55 A. A. Tahir, K. G. U. Wijayantha, S. Saremi-Yarahmadi, M. Mazhar and V. McKee, *Chem. Mater.*, 2009, **21**, 3763–3772.
56 M. W. Kanan and D. G. Nocera, *Science*, 2008, **321**, 1072–1075.
57 M. W. Kanan, Y. Surendranath and D. G. Nocera, *Chem. Soc. Rev.*, 2009, **38**, 109–114.
58 S. Kerisit and K. M. Rosso, *J. Chem. Phys.*, 2007, **127**, 124706.
59 N. Iordanova, M. Dupuis, and K. M. Rosso, *J. Chem. Phys.*, 2005, **122**, 144305.
60 J. Su, L. Guo, N. Bao and C. A. Grimes, *Nano Letters*, 2011, **11**, 1928-1933.
61 X. Zhang, F. Liu, Q.-L. Huang, G. Zhou and Z.-S. Wang, *J. Phy. Chem. C,* 2011, **115**, 12665-12671.
62 J. Krüger, Robert Plass, M. Grätzel, P. J. Cameron and L. M. Peter, *J. Phy. Chem. B*, 2003, **107**, 7536-7539.